Received: 3 July 2023 | Revised: 11 September 2023 | Accepted: 19 October 2023

DOI: 10.1002/qj.4612

Quarterly Journal of the Royal Meteorological Society RMetS

RESEARCH ARTICLE

Objective identification of tropical cyclone-induced remote moisture transport using digraphs

Shiqi Xiao[1] | **Aoqi Zhang**[1,2,3,4] | **Yilun Chen**[1,2,3] | **Weibiao Li**[1,2,3]

[1]School of Atmospheric Sciences, Sun Yat-Sen University, Zhuhai, China

[2]Key Laboratory of Tropical Atmosphere-Ocean System (Sun Yat-Sen University), Ministry of Education, Zhuhai, China

[3]Southern Marine Science and Engineering Guangdong Laboratory (Zhuhai), Zhuhai, China

[4]Key Laboratory of Flight Techniques and Flight Safety, CAFUC, Guanghan, China

Correspondence
Aoqi Zhang, School of Atmospheric Sciences, Sun Yat-Sen University, Zhuhai, China.
Email: zhangaoq3@mail.sysu.edu.cn

Funding information
Basic and Applied Basic Research Foundation of Guangdong Province, Grant/Award Number: 2020B0301030004; Innovation Group Project of the Southern Marine Science and Engineering Guangdong Laboratory (Zhuhai), Grant/Award Number: 311022006; National Natural Science Foundation of China, Grant/Award Numbers: 42005062, 42075004; Key Laboratory of Flight Techniques and Flight Safety, CAAC, Grant/Award Number: FZ2020ZZ03

Abstract

Tropical cyclone (TC)-induced remote moisture transport is the fundamental cause of TC-induced remote precipitation. However, despite increasing attention having been paid to TC-induced remote moisture transport over the past few decades, a method for the objective identification of TC remote moisture transport remains lacking, which is crucial to understanding the complex rainfall mechanisms associated with TC-induced remote moisture transport over recent decades. We set out to solve this issue in the present study by using a series of newly developed processing algorithms. Firstly, we identified vertically integrated water vapour transport (IVT) pathways using spatially smoothed moving window quantiles, and then used the maximum gradient method to segment IVT clusters from pathways. Relationship digraphs were constructed for IVT clusters to flexibly interpret the spatio-temporal merging and splitting processes among them. Finally, TC clusters (TCCs) and TC remote clusters (TRCs) were identified in succession based on the TC tracks and diagraphs of IVT clusters. Applications of these processing algorithms showed that the TCCs and TRCs at the same time step can be identified successfully by applying our method. The generality of the objective identification method was validated using data covering four decades. Our algorithms revealed discontinuous and uneven moisture transport, especially those associated with TCs, which benefits studies of remote rainfall associated with TCs. Furthermore, it facilitates the construction of IVT pathway and cluster datasets covering the past several decades, which can be used for analysing related characteristics and thereby revealing possible physical mechanisms underlying the nature of TRCs.

KEYWORDS

digraph, objective identification, remote moisture transport, tropical cyclone

1 | INTRODUCTION

Moisture transport pathways are mostly distributed in the lower troposphere, which plays a significant role in the global water cycle (Nayak and Villarini, 2017; Liu *et al.*, 2020; Fu *et al.*, 2021). Intense moisture transport has attracted the attention of scientists over the past few years because of its tight association with extreme heavy rainfall and subsequent flooding in continental regions located in the low and mid-latitudes (Ralph *et al.*, 2006; Pan and Lu, 2019). Algorithms have been developed and used for identifying moisture transport pathways, thereby enabling

the features, uncertainties and life cycles of these pathways to be quantified (Sellars *et al.*, 2017; Shearer *et al.*, 2020; Zhou *et al.*, 2021). Among all of the world's moisture transport pathways, atmospheric rivers (ARs) are the most dominant (Liu *et al.*, 2020). In previous studies, the vertically integrated water vapour transport (IVT) was chosen as a proxy, using absolute thresholds (e.g. 300, 500 or 700 $kg \cdot m^{-1} \cdot s^{-1}$), to reflect dynamic attributes of ARs (Gershunov *et al.*, 2017; Sellars *et al.*, 2017; Shields *et al.*, 2018; Shearer *et al.*, 2020), but was unable to identify local-scale extreme moisture transport at higher latitudes. Using relative thresholds like local quantiles (e.g. 85%) (Guan and Waliser, 2017; Pan and Lu, 2019) and threshold-free methods (Muszynski *et al.*, 2019; Xu *et al.*, 2020) on the IVT proxy, recent studies have been able to identify ARs at higher latitudes and even in the polar regions. In further progress, Pan and Lu (2020) divided a single moisture transport pathway into clusters, some of whose features were like tropical cyclones (TCs).

TCs are destructive weather systems that bring rain and flood-related hazards to coastal regions (Saha, 2015; Lu and Lall, 2017; Wang and Toumi, 2021) and even inland areas (Yang *et al.*, 2017; Zhang *et al.*, 2022). Besides their natural hazard potential, TCs are the third most dominant global moisture transport pathway, and play a substantial role in poleward moisture transport (Liu *et al.*, 2020, 2021; Li *et al.*, 2021). TCs are the most dominant extreme moisture transport in July–September in East Asia, where the precipitation in May–September exceeds 55% of the annual total (Liu *et al.*, 2022), as well as in North America (Jiang and Zipser, 2010; Guo *et al.*, 2017). In contrast to this consistency between these two regions in the period when TCs dominate, the peak period for ARs is June–July in East Asia (Kim *et al.*, 2020; Liang and Yong, 2020; Park *et al.*, 2021; Wang *et al.*, 2021) but December–February in North America (Nayak and Villarini, 2017). The interactions between TCs and ARs can contribute to strong and persistent poleward moisture transport and bring torrential rainfall to higher latitudes outside the region of TC circulation. In addition, this strong and persistent transport can also be triggered by the coupling of TCs and low-level jets (LLJs), resulting in heavy precipitation in areas remote from the TC itself (Ching *et al.*, 2014).

TC-induced remote moisture transport refers to a moisture transport pathway outside or outward from a TC's vicinity (roughly 500 km, depending on the size of the TC) but whose moisture transport source is the TC (Knaff *et al.*, 2014; Sun *et al.*, 2017; Yin *et al.*, 2022; Xu *et al.*, 2023). Such pathways of moisture transport are essential causes of torrential rainfall outside the TC's realm. Studies have found that the precipitation stemming from TC-induced remote moisture transport in South Korea (Byun and Lee, 2012; Baek *et al.*, 2013), Japan (Kodama and Satoh, 2022) and the United States (Galarneau *et al.*, 2010; Schumacher *et al.*, 2011; Moore *et al.*, 2013) results from the interaction between TCs and extratropical troughs and ARs (Cordeira *et al.*, 2013). Meanwhile, torrential rainfall in China attributable to TC-induced remote moisture transport has also attracted the attention of scientists. For instance, Typhoon *Vicente* (2012) brought extreme precipitation to Beijing through a remote moisture transport pathway (Wen *et al.*, 2015; Juan *et al.*, 2021). Sensitivity experiments using the Weather Research and Forecasting model found that *Vicente* played the most crucial role in this extreme precipitation in Beijing ($214\ mm \cdot day^{-1}$ in the urban area) via a strong moisture supply outside the TC's primary circulation and under the effects of the western North Pacific subtropical high and the midlatitude trough over Mongolia (Wen *et al.*, 2015; Juan *et al.*, 2021), but they neglected the role of Taiwan Island's topography. This is important because, by observing the vertical structure of remote moisture transport relative to the climatological mean, studies on TC *Mangkhut* (2018) have implied that Taiwan Island's topography played a substantial role in splitting part of *Mangkhut*'s moisture transport pathway passing east of the island like a watershed effect, bringing torrential rainfall to the Yangtze River Delta region (Yu *et al.*, 2020; Zuo *et al.*, 2022). However, they did not examine the absolute vertical composition of the remote moisture transport induced by the TC. In other works, the interactions among Typhoon *Infa* and *Cempaka* (2021), the subtropical high, extratropical systems, and local topography were found to have induced strong convergence of moisture from multiple sources below 850 hPa, bringing $600\ mm \cdot day^{-1}$ of rainfall to Henan Province in July 2021, which broke the record globally for the highest rate of daily precipitation observed by a continental meteorological station (Xu *et al.*, 2022; Yin *et al.*, 2022). Thus, it is clear that the complex interactions among TCs, topography, steering flow, weather systems, and the extreme precipitation associated with TCs can induce remote moisture transport.

TC-induced remote moisture transport is the fundamental cause of torrential rainfall due to its high complexity and uncertainty. However, all the studies mentioned above only identified remote moisture transport subjectively by examining figures, an approach that cannot systematically reveal the spatio-temporal characteristics of highly complex and uncertain TC-induced remote transport and the association with precipitation. To solve this issue, objective identification that can reflect moisture transport relationships is needed. In this regard, we developed an objective identification algorithm specifically for TCs and their remote moisture transport, including the identification, segmentation and construction of

spatio-temporal relations using moisture flux as the proxy. The algorithm was then applied to Typhoon *Mangkhut* (2018) to illustrate its method, step by step. The results from applying the method to TC-induced remote moisture transport are also presented. The rest of the article comprises four sections. Section 2 describes the data and explains the flowchart of their algorithmic processing. Section 3 provides further flowchart details in terms of validating each step of the algorithm, as well as some statistical aspects. Section 4 presents results from applying the method to all moisture transport in the period 1981–2020. And finally, Section 5 provides a summary and discusses implications for future studies.

2 | DATA AND METHODOLOGY

2.1 | Data

ERA5 is the fifth major global reanalysis produced by ECMWF (the European Centre for Medium-Range Weather Forecasts), the datasets of which include horizontal wind components, water vapour mixing ratio and geopotential height at multiple pressure levels, as well as the sea-level pressure (SLP) field at a single level, all at a spatial resolution of $0.25 \times 0.25°$ and temporal resolution of 1 hr (Hersbach *et al.*, 2020). We used the horizontal wind components and water vapour mixing ratio to compute the water vapour flux at each pressure level. The ERA5 meteorological fields in July–August–September (JAS) during 1981–2020 were retrieved at six-hourly resolution for derivation of the 40-year climatological mean and quantiles, as well as the different applications of the objective identification method (see Section 4) in this study, as JAS is the period with the highest TC frequency over the western North Pacific (Ren, 2002; Mei *et al.*, 2015; Guo *et al.*, 2017). Meanwhile, the ERA5 horizontal wind components and geopotential height were retrieved at an hourly resolution for moisture transport pattern identification and synoptic weather analysis during 1200 UTC 15 September 2018 to 0000 UTC 17 September 2018.

The best-track dataset for TCs during 1981–2020 was retrieved from the Shanghai Typhoon Institute of the China Meteorological Administration (CMA). The track dataset includes six-hourly TC positions, minimum sea-level pressure, and maximum wind speed throughout the life cycle of each TC over the western North Pacific (Ying *et al.*, 2014).

The Integrated Multi-satellitE Retrievals for Global Precipitation Measurement (IMERG) is an international satellite mission providing worldwide precipitation observational data, funded by the National Aeronautics and Space Administration (NASA) and the Japanese Aerospace Exploration Agency (Huffman *et al.*, 2020). The Global Precipitation Measurement Core Observatory design is an upgraded version of the widely used rain-sending package of the Tropical Rainfall Measuring Mission with a poleward extension of the observational range. We retrieved the half-hourly precipitation rate from the Final Precipitation L3 V06 product, with a spatial resolution of $0.1 \times 0.1°$, in JAS during 2001–2020.

2.2 | Methodology

Algorithms in previous studies were widely used to identify ARs by using IVT as the proxy (Pan and Lu, 2019; Xu *et al.*, 2020; Zhou *et al.*, 2021; Collow *et al.*, 2022). However, global moisture transport pathways, which is a broader concept consisting of ARs, LLJs, TCs, etc. (Liu *et al.*, 2020), can also be identified using IVT as the proxy. In this article, we define these patterns as IVT pathways.

Figure 1 is a flowchart showing the data processing steps that we followed in the objective identification of TCs, their remote moisture transport pathways, and their spatial relations and life cycles. *Step1* is the calculation of IVT. *Step2* involves calculating five-day moving window quantiles centred on the target date. *Step3* is spatial smoothing to obtain the threshold values of intensive moisture transport. *Step4* is the identification of IVT pathways (referred to as moisture transport pathways hereafter). *Step5* is the segmentation for each IVT pathway obtained from *Step4*. Each IVT pathway consists of at least one IVT cluster. *Step6* is the construction of a network that reflects IVT in/outflow relations among IVT clusters within an IVT pathway for each time step. *Step7* is the interpolation of TC tracks in ERA5 fields based on TC positions in CMA best-track data. *Step8* combines positions of interpolated TC tracks and that of maximum IVT within IVT clusters to identify TC moisture transport clusters (TCCs). *Step9* involves objectively identifying TC-induced remote moisture transport clusters (TRCs). *Step10* is the construction of life-cycle networks of IVT pathways and IVT clusters by comparing the areas of IVT pathways/clusters in the neighbouring time steps. These steps are further described in Section 3.

3 | ALGORITHMS AND VALIDATIONS

We begin in this section by reviewing the weather processes of *Mangkhut*. Then, we describe the identification of IVT pathways (Section 3.2: *Step1* to *Step4*), the identification of TCCs and TRCs using digraphs (Section 3.3: *Step5* to *Step9*), and the life cycles of IVT pathways/clusters

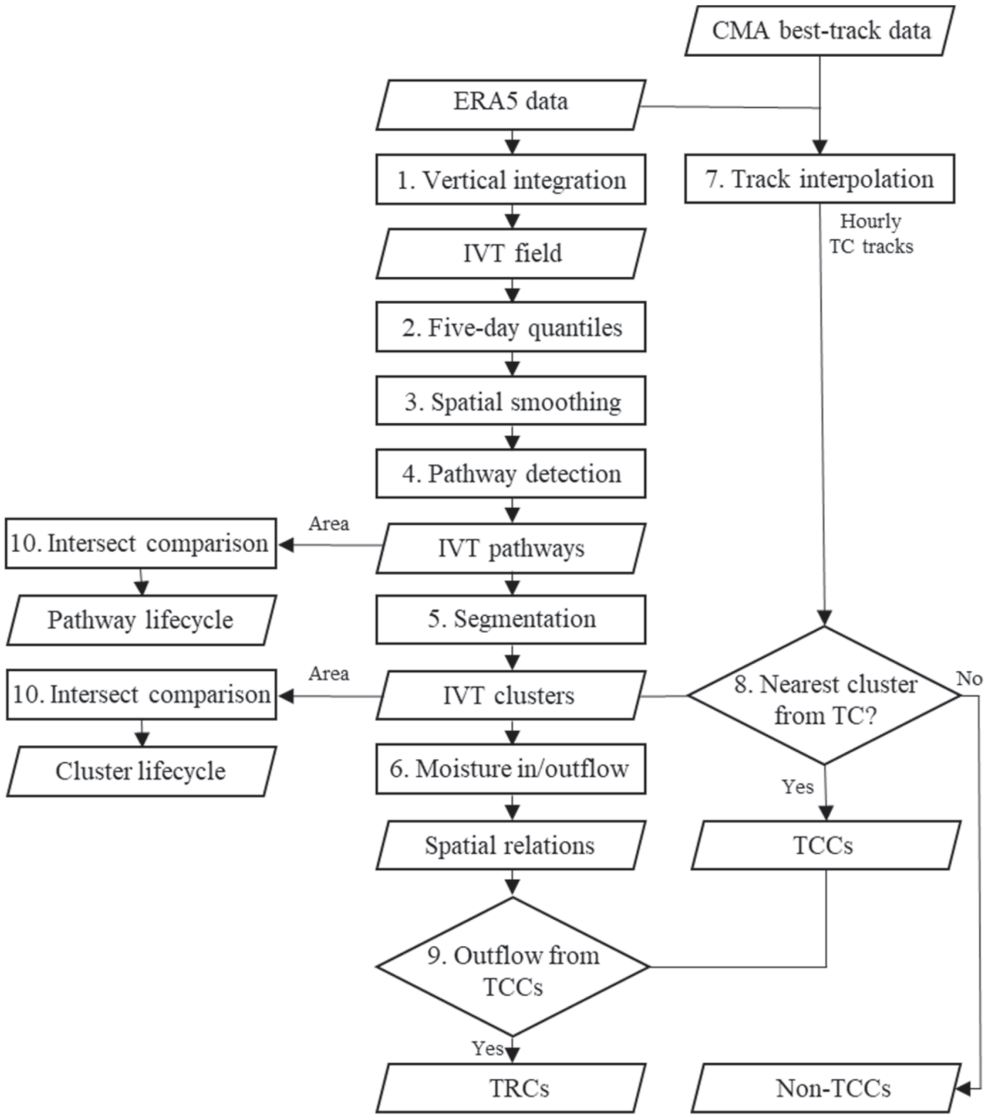

FIGURE 1 Flowchart of the objective identification of TRCs. Parallelograms represent input, intermediate and output data; rectangles represent data processing methods.

(Section: 3.4: *Step10*). Finally, we validate the methods using 40-year statistics (3.5).

3.1 | Overview of Typhoon *Mangkhut*

Typhoon *Mangkhut* formed on 7 September 2018 over the central Pacific and rapidly intensified to Super-Typhoon status on 11 September. It made landfall on Luzon Island at 1800 UTC 14 September and entered the South China Sea at 0000 UTC 15 September before then weakening to Strong Typhoon status (see Figure 2a). Typhoon *Mangkhut* approached and made landfall at Taishan, Guangdong Province, and brought torrential rainfall to the Pearl River Delta (PRD) region (dashed red box in Figure 2a), with 36 hr cumulative precipitation of 100–500 mm from 1200 UTC 15 September to 0000 UTC 17 September. Heavy precipitation also occurred over the Yangtze River Delta (YRD) region (dashed green box in Figure 2a) over the same period, with cumulative precipitation of 50–500 mm. Figure 2b shows the temporal evolution of hourly precipitation over the PRD and YRD regions. The mean hourly precipitation over the PRD (red line in Figure 2b) increased to a peak of 12.5 mm·hr^{-1} at 0600 UTC 16 September, and then decreased to 4 mm·hr^{-1} at 0000 UTC 17 September; while the mean hourly precipitation over the YRD (green line in Figure 2b) increased from less than 1 mm·hr^{-1} at 0500 UTC 14 September to 10 mm·hr^{-1} at 1700 UTC 16 September, before then decreasing to 5 mm·hr^{-1} on 17 September at 0000 UTC. All the results are consistent with previous studies (Yu *et al.*, 2020; Zuo *et al.*, 2022).

The temporal evolution of hourly precipitation and synoptic weather patterns surrounding Typhoon *Mangkhut* are shown in Figure 3. From 1800 UTC 15 September 2018 to 0000 UTC 17 September 2018, the rain belt in Typhoon *Mangkhut* approached the PRD (red) with the typhoon itself and brought torrential rainfall to the region with a maximum precipitation rate reaching

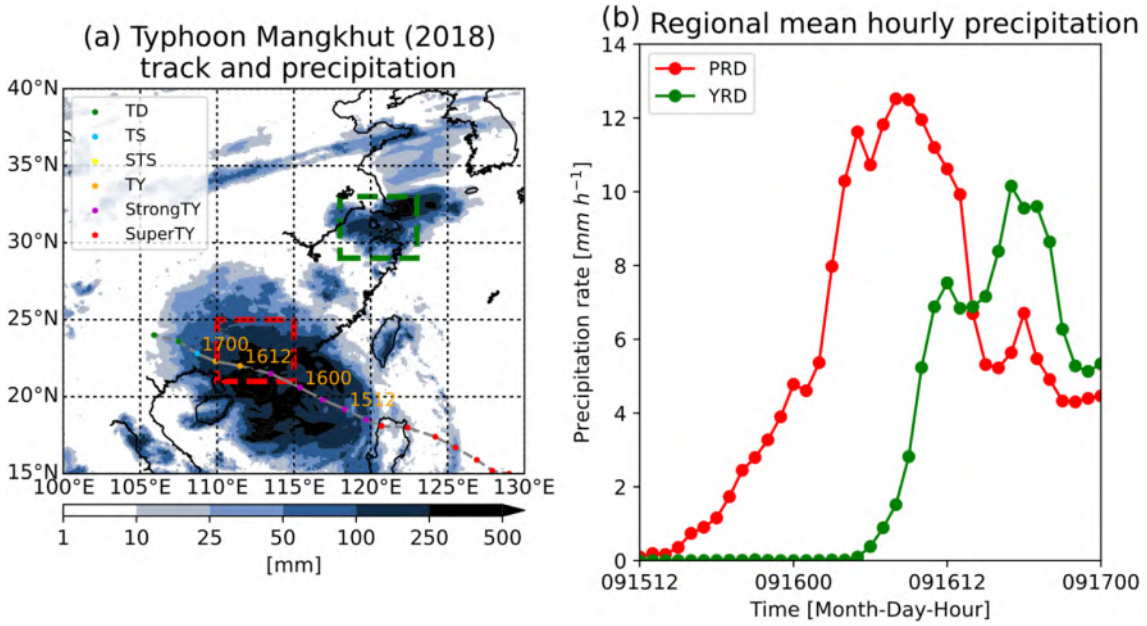

FIGURE 2 (a) The moving track of Typhoon *Mangkhut* (grey line) and horizontal distribution of cumulative precipitation (dark blue shading) from 1200 UTC 15 September to 0000 UTC 17 September. TD, Tropical Depression; TS, Tropical Storm; STS, Strong Tropical Storm; TY, Typhoon. (b) Hourly regional mean precipitation with time over the Pearl River Delta (PRD) (red line) and the YRD (green line). [Colour figure can be viewed at wileyonlinelibrary.com]

50 mm·hr^{-1} at 0600 UTC 16 September. *Mangkhut* moved from the southwest of Taiwan Island to the west from 1800 UTC 15 September to 0000 UTC 17 September due to the steering effect to the southwest of the subtropical high over 5880 gpm, changing the IVT at the east of Taiwan Island from northwestwards to northwards, which was parallel to the meridional orientation of Taiwan Island's topography (Figure S1).

Heavy precipitation began to develop to the north of Typhoon *Mangkhut* over the YRD at 0600 UTC 16 September and the precipitation rate reached 25 mm·hr^{-1} at 1800 UTC 16 September. The regions outside Typhoon *Mankghut* with 850 hPa wind speed exceeding 12 m·s^{-1} were almost all concentrated south of the YRD (green) until 1800 UTC 16 September, which implies the existence of LLJs (Chen and Tomassini, 2015; Gimeno *et al.*, 2016; Miao *et al.*, 2018). The area south of the YRD with 850 hPa wind speed exceeding 12 m·s^{-1} remained until 1200 UTC 16 September 2018 and gradually decreased with the increasing precipitation rate over the YRD. The direction of 850 hPa wind speeds exceeding 12 m·s^{-1} changed from southeasterly to southerly, which roughly followed the contours of 5880 and 5920 gpm at 500 hPa. The northwestern part of the 5880 and 5920 gpm contours retreated eastwards and became denser (larger pressure gradient force), causing higher wind speeds and a northward wind direction at 500 hPa to the northeast of Taiwan Island.

The torrential rainfall that fell over the YRD illustrates the role of moisture transport induced by *Mangkhut*. TC-induced moisture transport is the part of the IVT pathway outside or outward of the TC vicinity whose moisture transport source is the TC (Knaff *et al.*, 2014; Sun *et al.*, 2017; Yin *et al.*, 2022; Xu *et al.*, 2023). Consistent with Pan and Lu (2019), the intensity of TC-induced remote moisture transport should be larger than the Gaussian kernel smoothed 85% quantiles, depending on the time and region. Sections 3.2 to 3.4 document the identification of IVT pathways, of TCCs/TRCs, and the life cycles of IVT clusters. The methods employed in these sections are illustrated by taking *Mangkhut* as an example.

3.2 | Identification of IVT pathways

This section describes the processing algorithms of *Step1* (Section 3.2.1), *Step2* and *Step3* (3.2.2), and *Step4* (3.2.3), as in Figure 1, and the overall validation results (3.2.4).

3.2.1 | Integration of moisture transport

We used ERA5 data to calculate the IVT vectors from 1000 to 300 hPa in an Eulerian framework as the proxy in the IVT pathway (Pan and Lu, 2019):

$$\mathrm{IVT}_u = \frac{1}{g}\int_{1000\ \mathrm{hPa}}^{300\ \mathrm{hPa}} qu\ \mathrm{d}p, \tag{1}$$

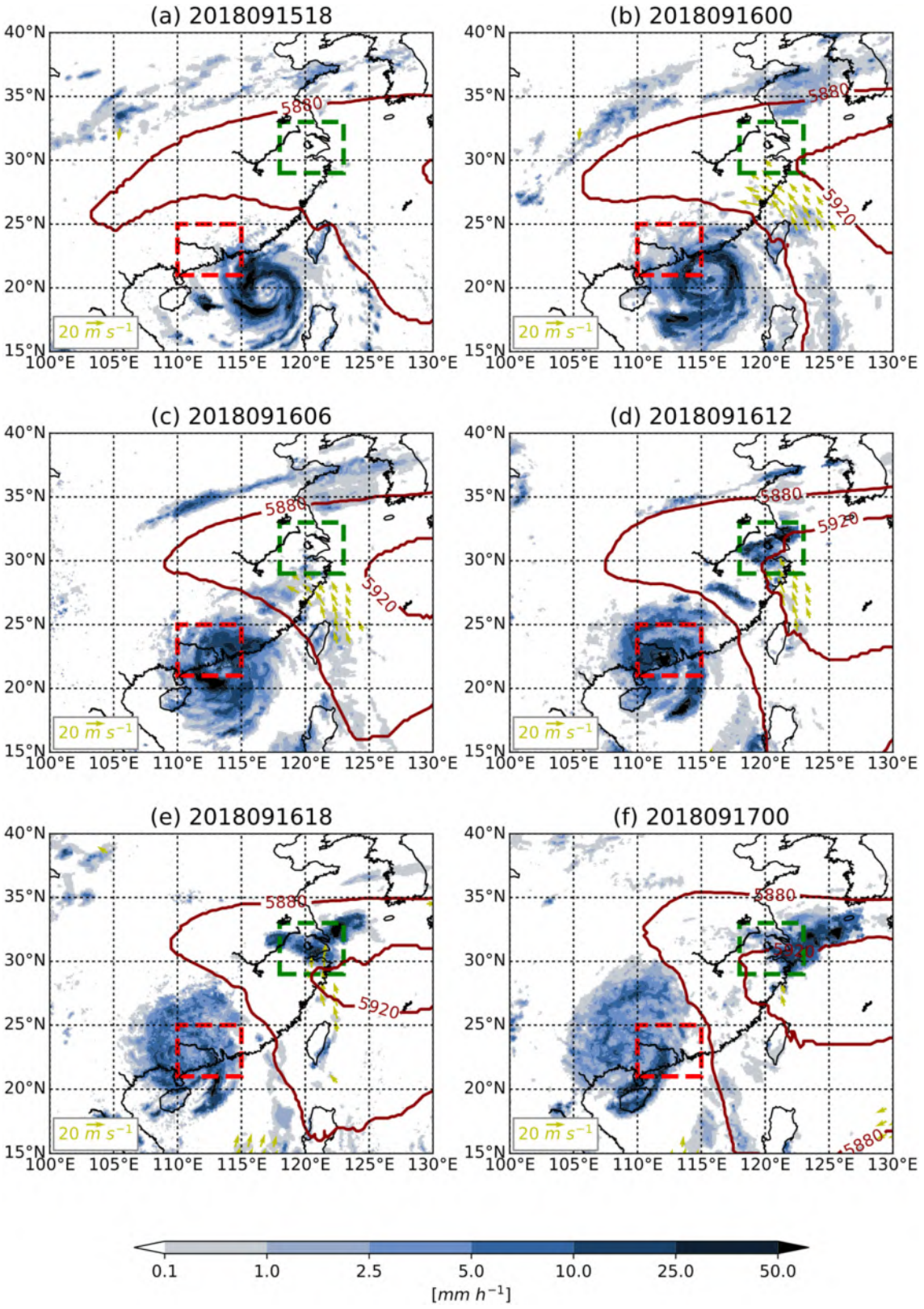

FIGURE 3 (a–f) Horizontal distributions of hourly precipitation overlaid with the 500 hPa geopotential height surrounding Typhoon *Mangkhut* from 1800 UTC 15 September 2018 to 0000 UTC 17 September 2018. The regions with 850 hPa wind speed over 12 m·s^{-1} outside *Mangkhut* are marked with yellow arrows. [Colour figure can be viewed at wileyonlinelibrary.com]

$$\mathrm{IVT}_v = \frac{1}{g}\int_{1000\ \mathrm{hPa}}^{300\ \mathrm{hPa}} qv\,\mathrm{d}p, \tag{2}$$

$$\mathrm{IVT} = \sqrt{\mathrm{IVT}_u^2 + \mathrm{IVT}_v^2}, \tag{3}$$

where IVT_u and IVT_v are the zonal and meridional components of the IVT vectors, respectively; IVT is the magnitude of the IVT vector; g is gravitational acceleration in $\mathrm{m{\cdot}s^{-2}}$; u and v are the layer-mean zonal and meridional wind components in $\mathrm{m{\cdot}s^{-1}}$, respectively; q is the layer-mean specific humidity in $\mathrm{kg{\cdot}kg^{-1}}$; and d$p$ is the pressure difference between two neighbouring pressure levels in Pa. Eastward (northward) zonal (meridional) components of IVT_u and IVT_v are defined as positive.

3.2.2 | Computation of IVT quantile thresholds

We used the five-day moving window quantiles centred on the target date and time (year, month, day, six-hourly: 0000, 0600, 1200, 1800 UTC) during 1981–2020 (see Equation (4)) to save on computational cost and increase the sample size of each local grid for quantile calculation. The quantile values change continuously with time in a year, showing a decreasing trend with significant undulation across the months (Figure S2). We use the Gaussian-kernel smoothed (GKS) quantiles as thresholds to identify regions with intensive moisture transport, as follows:

$$\mathrm{IVT}_{q,t_c,x,y} = \mathrm{quantile}_q\left(\mathrm{IVT}_{[1981,2020],[t_c-10\mathrm{d}t,t_c+10\mathrm{d}t],x,y}\right), \tag{4}$$

$$h(b_i) = d(x,y,x,y+b_i), \tag{5}$$

$$K(x,y,x_0,y_0,b_i) = -\frac{1}{\sqrt{2\pi}h}\mathrm{e}^{-\frac{d^2(x,y,x_0,y_0)}{2h^2(b_i)}}, \tag{6}$$

$$<\mathrm{IVT}_{q,t_c,x,y,b_i}> = \frac{\int\int_{x=x_0-75\mathrm{d}s,y=y_0-75\mathrm{d}s}^{x=x_0+75\mathrm{d}s,y=y_0+75\mathrm{d}s} K(x,y,x_0,y_0,b_i)\mathrm{IVT}_{q,t_c,x,y}\mathrm{d}x\mathrm{d}y}{\int\int_{x=x_0-75\mathrm{d}s,y=y_0-75\mathrm{d}s}^{x=x_0+75\mathrm{d}s,y=y_0+75\mathrm{d}s} K(x,y,x_0,y_0,b_i)\mathrm{d}x\mathrm{d}y}, \tag{7}$$

where (in Equation (4)) $\mathrm{IVT}_{q,t_c,x,y}$ is the grid-wise qth quantile (as q in quantile$_q$) of the IVT field across $10\times2+1=21$ time steps (5 days), with dt = 6 hr, and t_c referring to the centre of the date and time. The function $K(x,y,x_0,y_0,h)$ in Equation (6) is the Gaussian value; $d(x,y,x_0,y_0)$ is the geographical distance (geodistance, in km) between the longitude–latitude pair (x,y) and (x_0,y_0) in degrees equivalent to the bandwidth b_i (in degrees) for IVT pathway identification to calculate distance h in km in Equation (5) as standard deviation in Equation (6). We take 666.67 km equivalent to $b_i = 6°$, as in Equation (5) (Pan and Lu, 2019). Finally, we integrate the Gaussian values across the array with a size of $(75\times2+1)\times(75\times2+1)$ (that is, $[37.5°\times37.5°]$), with ds = 0.25°, as in Equation (7), to obtain the GKS local moving window qth IVT quantiles ($<\mathrm{IVT}_{q,t_c,x,y,b_i}>$) as thresholds.

3.2.3 | Identification of IVT pathways

In the remaining part of this study, the qth quantiles refer to $<\mathrm{IVT}_{q,t_c,x,y,b_i}>$ in Equation (7). Inspired by classifying the IVT pathways by using the intensity to represent the level of extreme moisture transport, we define an IVT pathway where IVT exceeds the 85% quantile ($q=0.85$) and the core IVT pathway corresponds to the 97.5% quantile ($q=0.975$). Those quantiles correspond to once and twice the standard deviation above the mean in a Gaussian (normal) distribution (single variable version in Equation (6), where d is the deviation of the value from the mean and h is the standard deviation). We compare the hourly IVT field with the nearest six-hourly (0000, 0600, 1200 and 1800 UTC) IVT quantile threshold field to identify contiguous IVT pathways. The IVT pathways are eliminated if less than 5% of them fall into the region of 0–50°N and 60°E–180° (Figure 4a–d), where the IVT pathways affecting East Asia form and develop over the Indian or Pacific Ocean.

The k-nearest neighbours refer to the fraction k of grid cells within a given IVT pathway that are the nearest to the given reference point (Pan and Lu, 2019). Starting from the grid cell of maximum IVT intensity within the IVT pathway, we move the reference point forward and backward with a fixed distance d along the weighted mean IVT direction of k-nearest neighbours to generate the trajectory for each IVT pathway in each time step. Pan and Lu (2019) set the weights of the k-nearest neighbours as a function of IVT and the minmax normalized geodistance between each neighbour and the reference grid divided by the sum of the weights of the k-nearest neighbours. The forward/backward search stops if less than 10% of k-nearest neighbour grid cells fall in front of (behind) the cross-section, which is perpendicular to the local trajectory direction at the reference point (Pan and Lu, 2019). In this study, we use $k = 0.3$ and $d = 50$ km instead of $d = 100$ km (Pan and Lu, 2019) for smoother trajectories. The features of each IVT pathway consist of area, length of the trajectory, width (area divided by length), cumulative IVT, mean IVT_v, and the area fraction of IVT cores (over the 97.5% quantile).

3.2.4 | Validation

The identification of moisture transport pathways is illustrated in Figure 4, wherein Figure 4a shows the

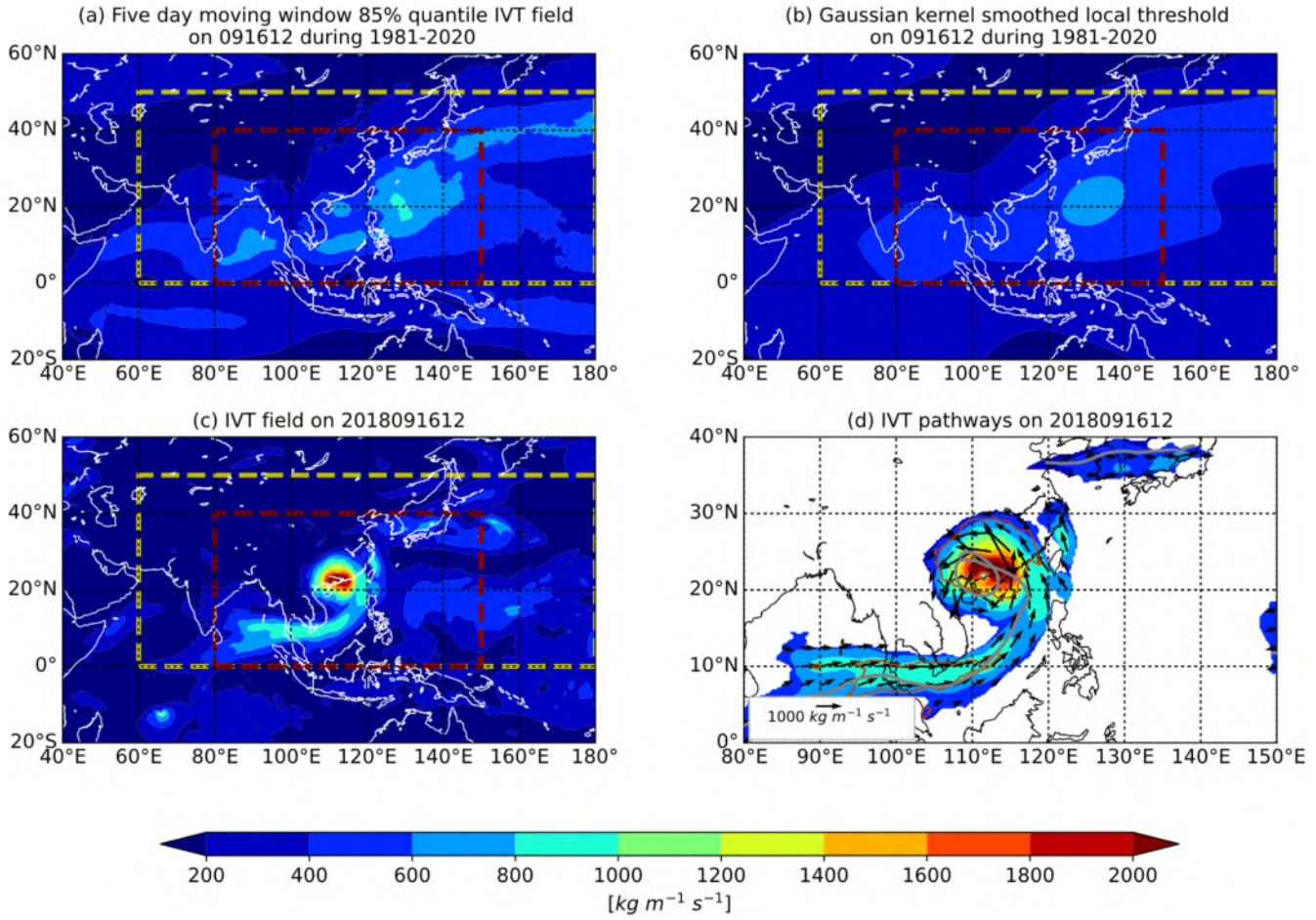

FIGURE 4 An instance of IVT pathway detection: (a) the five-day moving window 85% quantile IVT field centred at 1200 UTC 16 September during 1981–2020; (b) the local threshold after using Gaussian kernel smoothing; (c) the IVT field at 1200 UTC 16 September 2018; and (d) the detected IVT pathways with trajectories. The dashed yellow box is the IVT pathway selection region in which there is a likely effect on East Asia. The dashed dark-red box is the region surrounding TC *Mangkhut*. [Colour figure can be viewed at wileyonlinelibrary.com]

distribution of the local five-day moving window 85% quantile IVT field centred at 1200 UTC 16 September during 1981–2020. Five regions where IVT > 600 kg · m^{-1} · s^{-1} are distributed over the eastern North Indian Ocean, South China Sea, and western North Pacific, which is the typical moisture transport pathway that affects East Asia in the rainy season, consistent with previous studies (Pan and Lu, 2020; Cheng *et al.*, 2021; Dai *et al.*, 2021; Li *et al.*, 2021). We used the GKS to smooth the unevenly distributed quantiles in Figure 4a obtained in *Step2* to derive the local threshold as shown in Figure 4b obtained in *Step3*. For instance, all regions where IVT > 600 kg · m^{-1} · s^{-1} in Figure 4a shrink in Figure 4b as a result of GKS. Figure 4c shows the IVT fields at 1200 UTC 16 September 2018. Contiguous local grid cells where the values in Figure 4c are larger than in Figure 4b are identified as IVT pathways (see Figure 4d). For instance, the IVT pathways after elimination at 1200 UTC 16 September 2018 are displayed in Figure 4d, showing that the IVT at this time is larger (Figure 4c) than the corresponding local climatological thresholds (Figure 4b). The regions inside the brown contours are IVT cores (see Figure 4d) that are inside IVT pathways, where the moisture transport is more intense from a local quantile perspective. The orientations of these trajectories (grey lines) almost follow their surrounding IVT vectors (black arrows), showing the validity of the trajectory generation in Figure 4d.

3.3 | Identification of TCCs and TRCs using digraphs

This section describes the processing algorithms of *Step5* (Section 3.3.1), *Step6* (3.3.2), *Step7* and *8* (3.3.3), and *Step9* (3.3.4), as in Figure 1, and their overall validation (3.3.5).

3.3.1 | Segmentations of IVT pathways

We take the distance $h = 111.11$ km, equivalent to segmentation bandwidth $b_s = 1°$, as the standard

deviation to compute the GKS IVT magnitudes $\overline{< \mathrm{IVT}_{q=0.85,t_c,x,y,b_s=1^\circ} >}$ following Equations (5)–(7) as the proxy to divide the IVT pathways into clusters using the maximum gradient method (Chen *et al.*, 2020). The bandwidth sensitivity test shows that $b_s = 1^\circ$ has the largest proportion (70%) of IVT clusters with sizes typical of TCs (Figure S3). The algorithm of maximum gradient method on the proxy is as follows:

a. Search all grid cells satisfying the condition that the IVT at the eight nearest grid cells is smaller than at the given grid cells. These grid cells are called local maxima grid cells. Then, we assign a cluster value to each local maxima grid cell (a positive integer).
b. For each non-maxima grid cell inside an IVT pathway, search the nearest eight grid cells and find the one with the maximum IVT gradient among the eight.
c. Repeat *Step5.b* until the local maximum is found. Assign a cluster value to all grid cells along the search path.
d. For two clusters whose distance between their own local maxima is smaller than 500 km, merge the cluster with the smaller local maxima into the cluster with the larger maxima. For clusters with an area smaller than 40,000 km^2 (small), find the cluster with the closest distance between its maximum and the smaller cluster's maximum for merging.

The various coloured IVT clusters in Figure 5b at 0000 UTC 16 September 2018 are the outputs of the above algorithm. Each IVT pathway consists of at least one IVT cluster. There are two advantages of IVT clusters that are obtained from the maximum gradient method. The first is that the mismatch between IVT clusters in two neighbouring time steps due to the merging and splitting processes is resolved (see Section 3.4.1), which is convenient for constructing a spatio-temporal relation among IVT clusters. The second is that the position of maximum IVT is located several grids away from the border of the cluster, which implies a concentration of moisture transport. The method to generate trajectories and features for each IVT pathway also applies to each IVT cluster and combinations of contiguous IVT clusters.

3.3.2 | Spatial relations among clusters

The IVT clusters obtained from *Step5* correspond to connected domains with directed relations, so we use the directed graph concept (hereafter "digraph") in mathematics to reflect the relationships among them. In this study, the directed edge connects two nodes such that there is IVT flux from the first cluster to the second node. Directed edges are constructed to reflect cross-cluster moisture transport among the clusters based on the spatio-temporally smoothed IVT obtained in *Step5*. The digraph $G = (V, E)$ consists of a set of vertices (nodes) V that represents objects and a set of directed edges E, where each element of E connects an ordered pair of nodes, pointing from the first node to the second node in the pair.

For each time step, we construct digraphs inside an IVT pathway through the following steps:

a. Set the positions of nodes that represent IVT clusters at the positions of their IVT maxima. For IVT pathways that consist of only one IVT cluster, skip the remaining steps.
b. For each IVT cluster A, calculate the mean IVT vector. Find all the neighbouring clusters and form the set $\{B'\}$. For each cluster B_i in $\{B'\}$, calculate the grid-wise moisture transport component that is perpendicular to the border between cluster A and B_i, which is obtained by applying the Sobel gradient operator (Kanopoulos *et al.*, 1988; Vincent and Folorunso, 2009; Gao *et al.*, 2010) on the masks (Figure S4) of the two clusters above. Gradients are generated using the opencv2 software package (Howse, 2013) in the Python programming language.
c. For each IVT cluster B_i that receives moisture flow from cluster A, assign the directed edges pointing from node A to node B_i.

3.3.3 | Identification of TCCs based on interpolation

Recent research has established that the proximity between the TC tracks in the best-track dataset and those in reanalysis datasets is generally within 150 km (Xu *et al.*, 2016). Importantly, this distance is significantly smaller than the typical radius of TC primary circulation (Willoughby, 1990; Wang Bin *et al.*, 1999; Mallen *et al.*, 2005). To interpolate the CMA best-track with the ERA5 SLP field, which possesses only one minimum in the TC primary circulation, we employ the following interpolation techniques:

a. In each hourly time step, we identify the ERA5 grid cells that were spatially and temporally closest to the CMA best-track TC position every 6 hr. We initialized the position of the grid cells accordingly. By iteratively moving the grid cell to one of its eight neighbouring cells with the most negative SLP gradient, we continued until it reached the local minimum in the ERA5 SLP field. This process concluded the interpolation of TC tracks.

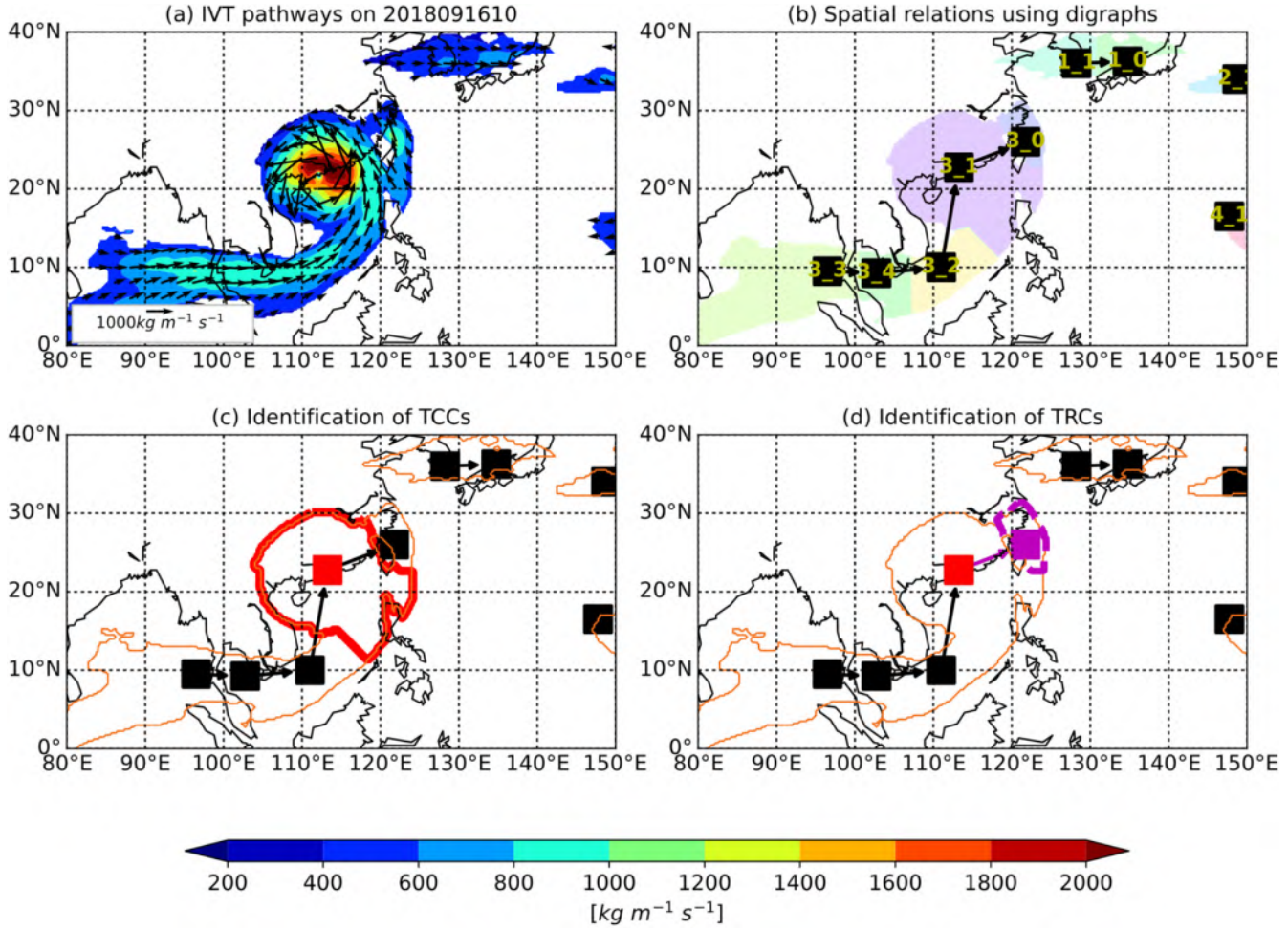

FIGURE 5 The instance of tropical cyclone clusters (TCC) and tropical remote clusters (TRC) identification at 1000 UTC 16 September 2018 for *Mangkhut* and its surroundings: (a) IVT field of IVT pathways; (b) IVT clusters (in different colours) obtained in *Step5*, with digraphs obtained in *Step6* marked as black nodes (labelled in yellow) and black directed edges. (c) Identification of TCCs (red contours) and the borders of IVT pathways (orange). (d) Identification of the TRC (dashed magenta contour). [Colour figure can be viewed at wileyonlinelibrary.com]

b. For each time step and for all clusters of all IVT pathways, the nearest cluster to the TC track is identified as the TCC.

3.3.4 | Identification of TRCs

Following the definition of TC-induced remote moisture transport, TRCs are identified as moisture transport clusters outside the TC but receiving moisture outflow from TCCs. For a given time step, we select all nodes that correspond to their TC clusters to form a set, $V_{TC} = \{n_{TC1}, n_{TC2}, \ldots n_{TCn}\}$. For each node n_{TCi}, where $i = \{1, 2, \ldots, n\}$ that belongs to V_{TC}, find all reachable nodes along directed edges starting from node n_{TCi}, then exclude the nodes of TCCs and the nodes that are at least four nodes away from the nearest TCCs. The nodes representing TRCs directly or indirectly receive moisture outflow from corresponding TCCs according to digraphs obtained in *Step6*.

3.3.5 | Validation

Figure 5 shows the implementation of *Step5* to *Step9* with Typhoon *Mangkhut*, wherein Figure 5a shows a detailed view of the IVT pathways at 1000 UTC 16 September 2018 inside the dashed dark-red box in Figures 4, and 5b shows the different coloured IVT clusters obtained in *Step5*. The spatial relations among the IVT clusters within IVT pathways are constructed using digraphs with labelled black nodes and black edges. The label $m - n$ means the IVT pathway number m and its IVT cluster number n for illustration of *Step6*, *Step8* and *Step9*. For instance, the digraph for IVT pathway 3 shows that moisture flows from cluster 3-3 (Bay of Bengal) to clusters 3-4, 3-2, 3-1

and finally 3-0. Figure 5c shows that IVT cluster 3-1 is the nearest to the interpolated TC track (21°N, 115.25°E) among the clusters, and thus the contour of the cluster and the node are marked red to represent the cluster of Typhoon *Mangkhut* (TCC–Mangkhut) at 1000 UTC 16 September 2018. Figure 5d shows the identification of the TC-induced remote IVT cluster, marked by the magenta node and dashed magenta contour, based on the identified TC cluster in Figure 5c and the digraph (see Figure 5b). We selected TCC–Mangkhut (3-1 in Figure 5c,d), found the IVT cluster 3-0, and marked the cluster and the node in magenta (see Figure 5d) to represent the remote IVT cluster induced by Typhoon *Mangkhut* (TRC–Mangkhut). Another example of TRC identification in multiple TC cases is illustrated in Figure S5.

3.4 | Temporal evolution

3.4.1 | Life cycles of IVT pathways/clusters

We use digraphs to reflect the life cycles of IVT pathways in the dimension of time (as per *Step10* in Figure 1). Also, we use the area of two IVT pathways at neighbouring time steps and that of their intersection to add nodes and directed edges. The advantage of this life-cycle generation method is the flexibility to identify merging and splitting of IVT pathways with time. This algorithm also applies to IVT clusters at any two neighbouring time steps.

3.4.2 | Validation

The spatio-temporal evolutions of IVT pathways and their clusters based on digraphs, and the features of the IVT pathway containing TCC–Mangkhut (red) and TRC–Mangkhut (magenta) are shown in Figure 6. The IVT pathway containing TCC–Mangkhut exists during 1800 UTC 15 September to 0000 UTC 17 September. TRC–Mangkhut formed at 2300 UTC 15 September (first dashed blue line) and separated completely from the IVT pathway containing TCC–Mangkhut, merging into the green IVT pathway over Korea and Japan at 1700 UTC 16 September (third dashed blue line). This separation cut off the moisture supply from Typhoon *Mangkhut*, likely due to the overly long distance between TCC– and TRC–Mangkhut east of Taiwan Island as a result of the west-northwestward translation of Typhoon *Mangkhut* (see Figure 2a and Figure 6a–f), and the meridionally oriented topography of Taiwan Island only preserving meridional moisture transport parallel to the topography (Chen *et al.*, 2010; Tang and Chan, 2014). This cut-off effect is one of the reasons why the hourly precipitation rate over the YRD peaked simultaneously and decreased afterwards (see Figure 2b). The splitting of IVT pathways (green in Figure 6g) into two at 0000 UTC 16 September, the merging of TRC–Mangkhut into the green IVT pathway over Korea and Japan at 1700 UTC, and the merging of the two green IVT pathways into one at 2200 UTC, validate the robustness of the spatio-temporal relations of IVT pathways/clusters using digraphs (see Figure 6a–g).

The area of TRC–Mangkhut (magenta) decreased sharply from 280,000–300,000 km^2 at 1700 UTC 16 September to 50,000 km^2 at 0000 UTC 17 September (the last dashed blue line in Figure 6h). Although the trajectory length (grey lines in Figure 6a–f) increased mildly from 600 to 800 km from 1800 UTC 15 September to 2300 UTC 16 September, the length decreased sharply from 800 to 300 km at 0000 UTC 17 September, which completely reversed the previous increase; the width of TRC–Mangkhut decreased over its lifetime (Figure 6i). The grid-wise sum of IVT over the IVT pathway containing TCC–Mangkhut (red) and that of TRC–Mangkhut (magenta) decreased over the lifetime of TRC–Mangkhut. In contrast, the fraction of northward-transport grid cells over TRC–Mangkhut remained at more than 0.95, which was much higher than that of the IVT pathway containing TCC–Mangkhut (0.7–0.8). The mean meridional moisture transport over TRC–Mangkhut was 500–600 $kg \cdot m^{-1} \cdot s^{-1}$, which was larger than the 200–300 $kg \cdot m^{-1} \cdot s^{-1}$ over the IVT pathway containing TCC–Mangkhut until 1700 UTC 16 September. The area fraction of IVT cores decreased, except for a sudden rebound from 0.04 to 0.1 from 0900 to 1000 UTC 16 September (second dashed blue line in Figure 6m).

4 | APPLICATIONS

4.1 | Frequency statistics

We used this objective identification method to analyse the frequency of IVT clusters over JAS during 1981–2020. Over western North Pacific and surroundings, 269,521 IVT clusters, 14,537 TCCs and 7,228 TRCs are identified over JAS during 1981–2020. The numbers of TCCs and TRCs are 5.39% and 2.68% of all IVT clusters, respectively. The peaks of IVT cluster frequency (including TCC and TRC; see Figure 7a) show one peak over the South China Sea up to 40%. There are also peaks in southern China, northeastern China, and the ocean surrounding Japan, up to 20%. The IVT frequency patterns are consistent with the climatological AR frequency in the late summer monsoon season in previous studies (Kim *et al.*, 2020; Park *et al.*, 2021; Xiong and Ren, 2021). The frequency of TCCs in JAS peaks over the ocean east of the Philippines and Taiwan, and

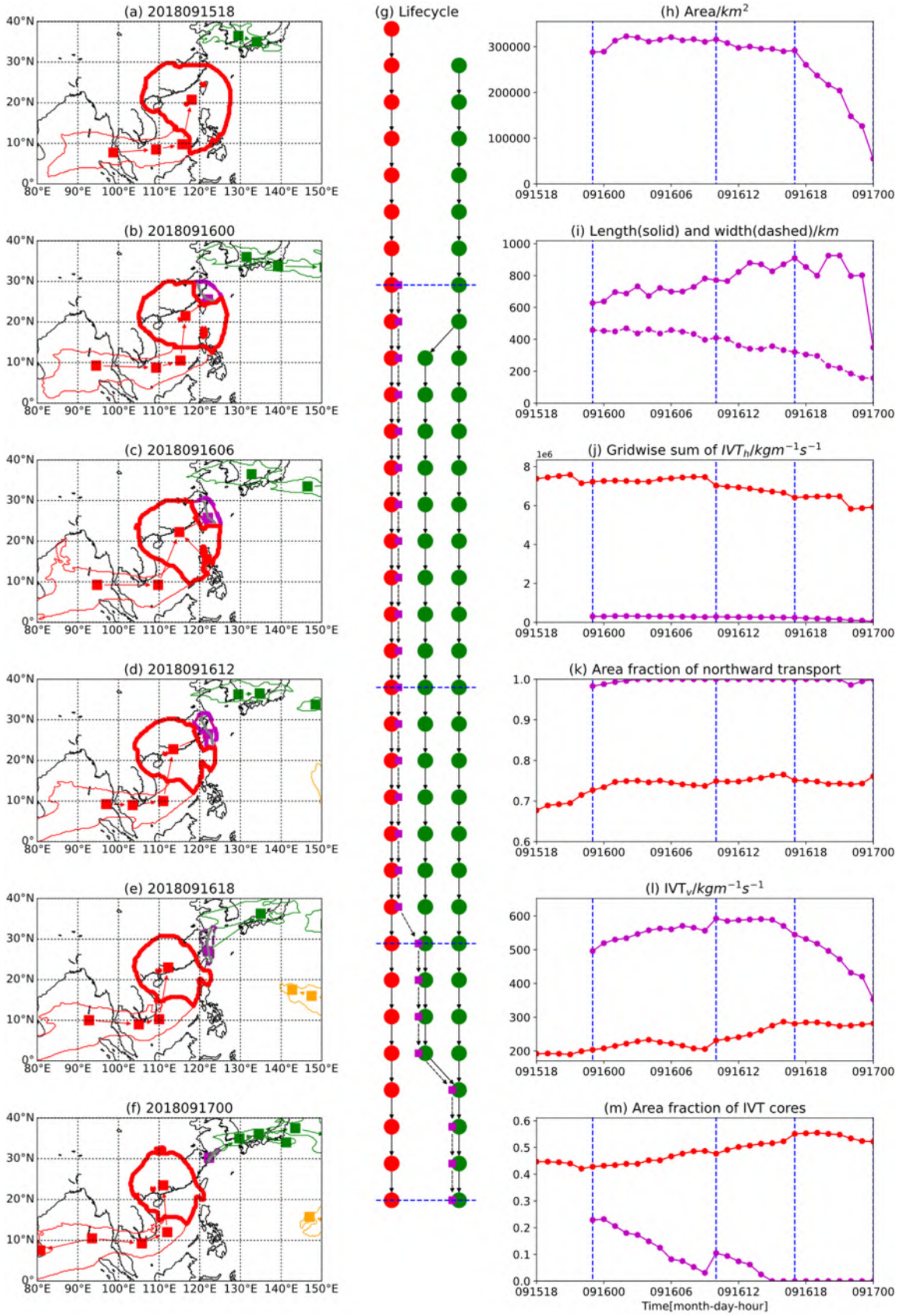

FIGURE 6 (a–f) Horizontal distribution of IVT clusters. (g) Life cycles of IVT clusters. (h–m) Time series of key parameters. Red: IVT pathway containing TCC–Mangkhut; green: IVT pathways that TRC–Mangkhut (magenta) merged into; blue: key time steps. [Colour figure can be viewed at wileyonlinelibrary.com]

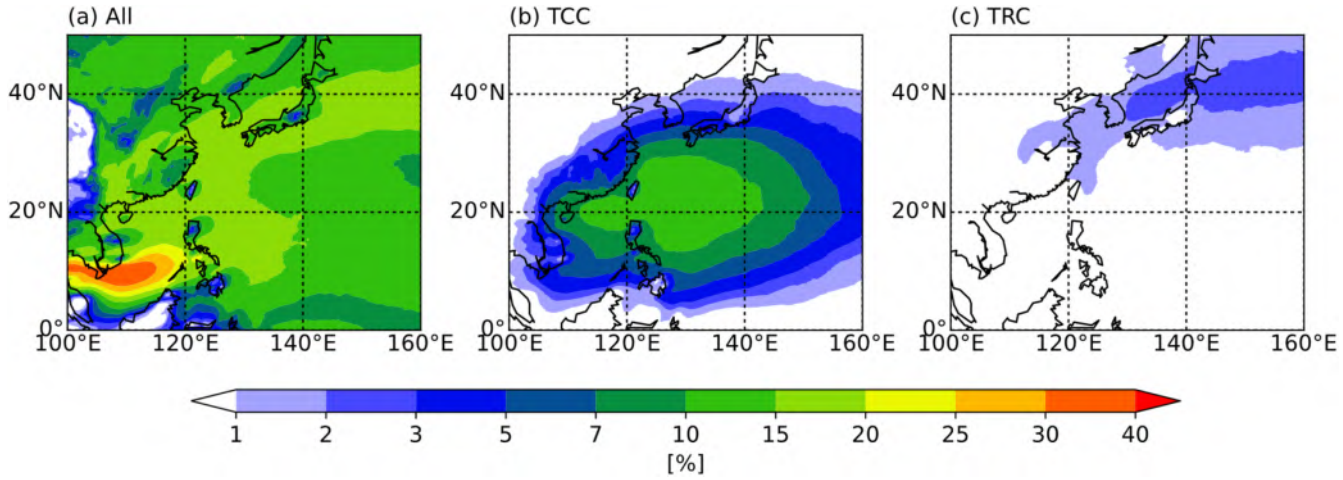

FIGURE 7 Frequency of (a) all IVT clusters, (b) TCC and (c) TRC, in JAS during 1981–2020. [Colour figure can be viewed at wileyonlinelibrary.com]

over China, reaching 15%; and Guangdong in China is the region where the TCC frequency is the highest over land, reaching 10%, which is consistent with the TC track density reported in previous studies (Manganello *et al.*, 2012; Strachan *et al.*, 2013; Mei *et al.*, 2015). The frequency of TRCs (see Figure 7c) is lower than 4%. The patterns of TRC frequency are like that of the IVT frequency in JAS. In terms of land areas, northeastern China, South Korea, northern Japan and central China are the regions with the highest TRC frequency, at up to 3%. The low (4%) but non-negligible TRC frequency, which is consistent with that of IVT, is the likely reason behind the increasing level of attention paid to TC-induced remote moisture transport over the past few decades.

4.2 | Area of IVT clusters and association with six-hourly precipitation

We applied the objective identification method to the relationship between the area of IVT clusters and the associated cluster-wide average six-hourly total precipitation (see Figure 8) during 2001–2020. Figure 8a shows the gradual increase in six-hourly total precipitation with the area of IVT clusters among 56,835 rainy IVT clusters of 142,164 during 2001–2020. The number of rainy TCCs are 6,950, less than 12% of all rainy IVT clusters. Median precipitation increases more steeply with the area of TCCs with the peak at an area of $80–250 \times 10^4$ km^2 (see Figure 8b) and has a more spread-out distribution compared to that of all IVT clusters. There are only 2,917 rainy TRCs, less than half of rainy TCCs and 2.05% of all IVT clusters, showing the scarceness of TC-induced remote moisture transport and lower fraction of rainy TRCs (2,917/3,615 ≈ 80.7%) over all TRCs compared to that of TCCs (6,950/7,239 ≈ 96.0%). Although the precipitation increases less steeply with the area of TRCs (see Figure 8c), there are TRCs with heavier precipitation than that of TCCs, with an area of $30–50 \times 10^4$ km^2, implying precipitation extremes over TRCs. Moreover, the distribution of precipitation over TRCs is more spread-out (higher probability of low and high precipitation) than that of IVT clusters and TCCs, implying high uncertainty of complexity of rainfall mechanisms over TRCs. Our objective identification method could provide a systematic means to find associations between the geometric features of IVT clusters and precipitation, which would be beneficial for finding the causes and mechanisms underlying this association, especially useful for highly uncertain and complex rainfall mechanisms over TRCs.

5 | DISCUSSION AND CONCLUSIONS

In this study, we developed a series of objective identification algorithms for TCCs and TRCs based on the concept of TC-induced remote moisture transport. These algorithms were applied to JAS during 1981–2020 over the western North Pacific and surrounding regions using ERA5 and CMA best-track data. The main achievements can be summarized as follows:

- We used the GKS five-day moving window 85% quantiles as thresholds, with a standard deviation distance equivalent to $b_i = 6°$, to identify IVT pathways and feature generation (Pan and Lu, 2019). The threshold values were obtained from five-day moving window quantiles during 1981–2020, which changed continuously with time steps.

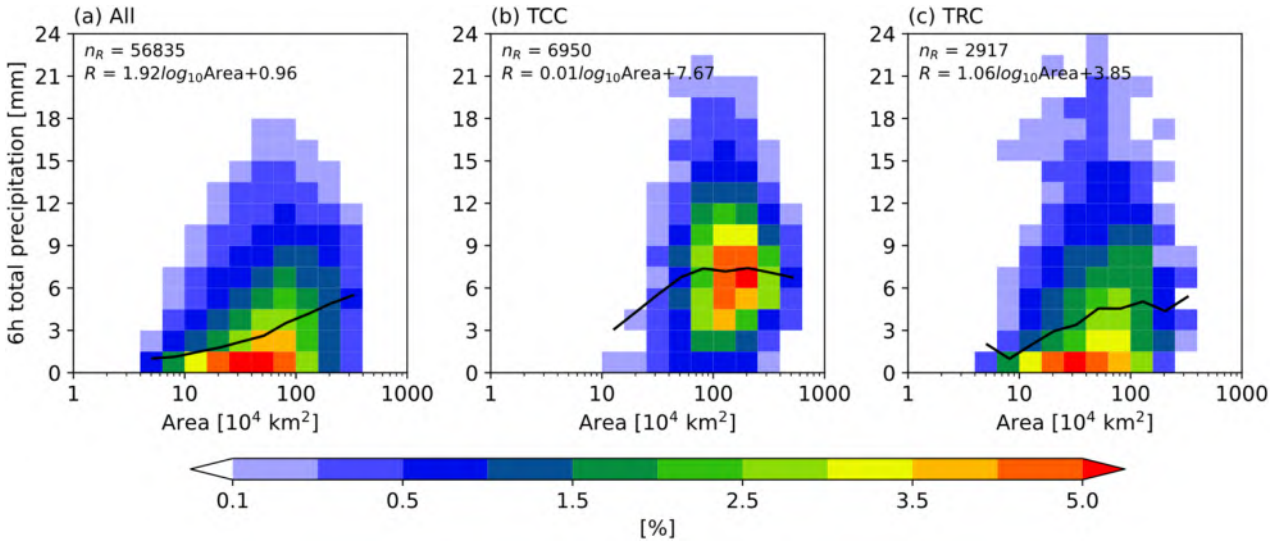

FIGURE 8 Two-dimensional histograms of area versus six-hourly total precipitation associated with (a) IVT (clusters), (b) TCCs and (c) TRCs, in JAS during 2001–2020. Black lines: median precipitation. Upper-left: $\boldsymbol{n_R}$: samples with precipitation; $\boldsymbol{R}$: six-hourly total precipitation. [Colour figure can be viewed at wileyonlinelibrary.com]

- We used the maximum gradient method to segment IVT pathways into IVT clusters (Chen *et al.*, 2020). We conducted sensitivity experiments for the segmentation bandwidth (standard deviation) and set it as 111.11 km (around 1°). Spatial digraphs were constructed to reflect the spatial relations among the IVT clusters using the Sobel gradient operator. TCCs were then identified using TC track data; TRCs were identified based on digraph relations of TCCs.
- Temporal digraphs were also constructed to reflect the life cycles of IVT clusters. The combination of spatial and temporal diagraphs was able to adequately resolve the merging and splitting processes of IVT clusters including TCCs and TRCs.
- We used the objective identification method to analyse spatial frequency patterns of IVT clusters, TCCs and TRCs in JAS during 1981–2020 for validation, and found a high degree of consistency with previous studies.
- The association between the area of IVT clusters, TCCs and TRCs and six-hourly total precipitation was analysed statistically using the objective identification method. The outliers of heavy precipitation of TRCs validated the need to find mechanisms underlying the cluster–precipitation association.

As the first objective identification method of TC-induced remote moisture transport, the main advantages and innovations of the method include the following:

- We propose GKS five-day moving window 85% quantiles to flexibly identify IVT pathways. Thus, the thresholds change continuously with time steps and avoid sudden changes across months.
- We use the maximum gradient method to segment IVT pathways into clusters. The moisture transport intensities are larger inside and smaller at the border in the identified clusters, which reflects well the physical foundation of discontinuous and uneven moisture transport.
- We innovatively introduce the concept of digraphs to characterize moisture transport relations among IVT clusters. These digraphs should facilitate future studies regarding the role of moisture transport in remote rainfall associated with TCs. It can also resolve merging and splitting processes and is therefore of benefit to investigations into the life cycles of TCCs and TRCs.

The construction of digraph-based datasets of TCCs and TRCs over the past several decades is being undertaken using this objective identification approach, which will facilitate further studies on the characteristics and mechanisms of TC-induced moisture transport and precipitation.

Despite these encouraging findings and foundations for future work, it is important to acknowledge that there are some limitations and uncertainties, as follows. The series of algorithms was only validated with TC effects over the western North Pacific and its surrounding regions (including the northern Indian Ocean). Also, the level of error in the method may increase in cases of more than two TCs with overlapping remote moisture transport pathways. Thus, it would be a benefit to studies on the moisture transport associated with binary TCs if the limitations

above could be solved (Ren *et al.*, 2020). Accordingly, we should carefully check cases of two neighbouring TCs at the same time step. Some TCCs are asymmetric, as they are connected to moisture transport pathways outside of the TC. However, we intend to uncover more characteristics of TCCs and TRCs in the future to further understand the mechanisms underlying TC-induced remote moisture transport.

FUNDING INFORMATION

This research was funded by the National Science Foundation of China (grant no. 42075004 and 42005062), the Guangdong Major Project of Basic and Applied Basic Research (grant no. 2020B0301030004), the Key Laboratory of Flight Techniques and Flight Safety, CAAC (grant no. FZ2020ZZ03), and the Innovation Group Project of the Southern Marine Science and Engineering Guangdong Laboratory (Zhuhai) (grant no. 311022006).

CONFLICT OF INTEREST STATEMENT

The contact author has declared that none of the authors have competing interests.

DATA AVAILABILITY STATEMENT

ERA5, IMERG, CMA best-track data, and the DEM topography data (supplementary material) are available from the following websites: https://cds.climate.copernicus.eu/cdsapp#!/search?type=dataset&text=ERA5, https://disc.gsfc.nasa.gov/datasets/GPM_3IMERGHH_06/summary?keywords=%22IMERG%20final%22, https://tcdata.typhoon.org.cn/en/zjljsjj.html and https://www.ngdc.noaa.gov/mgg/global/relief/ETOPO2/ETOPO2v2-2006/ETOPO2v2c/netCDF/ETOPO2v2c_f4_netCDF.zip.

ORCID

Shiqi Xiao https://orcid.org/0009-0009-4589-4339

REFERENCES

Baek, E.-H., Kim, J.-H., Kug, J.-S. & Lim, G.-H. (2013) Favorable versus unfavorable synoptic backgrounds for indirect precipitation events ahead of tropical cyclones approaching the Korean Peninsula: A comparison of two cases. *Asia-Pacific Journal of Atmospheric Sciences*, 49, 333–346.

Byun, K.-Y. & Lee, T.-Y. (2012) Remote effects of tropical cyclones on heavy rainfall over the Korean peninsula – statistical and composite analysis. *Tellus, Series A: Dynamic Meteorology and Oceanography*, 64, 14983.

Chen, J.-M., Li, T. & Shih, C.-F. (2010) Tropical cyclone– and monsoon-induced rainfall variability in Taiwan. *Journal of Climate*, 23, 4107–4120.

Chen, R. & Tomassini, L. (2015) The role of moisture in summertime low-level jet formation and associated rainfall over the east Asian monsoon region. *Journal of the Atmospheric Sciences*, 72, 3871–3890.

Chen, Y., Chen, G., Cui, C., Zhang, A., Wan, R., Zhou, S. et al. (2020) Retrieval of the vertical evolution of the cloud effective radius from the Chinese FY-4 (Feng Yun 4) next-generation geostationary satellites. *Atmospheric Chemistry and Physics*, 20, 1131–1145.

Cheng, T.F., Lu, M. & Dai, L. (2021) Moisture channels and pre-existing weather systems for East Asian rain belts. *NPJ Climate and Atmospheric Science*, 4, 1–13.

Ching, J., Rotunno, R., Lemone, M., Martilli, A., Kosovic, B., Jimenez, P.A. et al. (2014) Convectively induced secondary circulations in fine-grid mesoscale numerical weather prediction models. *Monthly Weather Review*, 142, 3284–3302.

Collow, A.B.M., Shields, C.A., Guan, B., Kim, S., Lora, J.M., McClenny, E.E. et al. (2022) An overview of ARTMIP's tier 2 reanalysis intercomparison: uncertainty in the detection of atmospheric rivers and their associated precipitation. *Journal of Geophysical Research-Atmospheres*, 127, e2021JD036155.

Cordeira, J.M., Ralph, F.M. & Moore, B.J. (2013) The development and evolution of two atmospheric rivers in proximity to Western North Pacific tropical cyclones in October 2010. *Monthly Weather Review*, 141, 4234–4255.

Dai, X., Yang, Y. & Wang, P. (2021) Asian monsoon projection with a new large-scale monsoon definition. *Theoretical and Applied Climatology*, 147, 1003–1013.

Fu, Y., Chen, Y., Zhang, X., Wang, Y., Li, R., Liu, Q. et al. (2021) Fundamental characteristics of tropical rain cell structures as measured by TRMM PR. *Journal of Meteorological Research*, 34, 1129–1150.

Galarneau, T.J., Jr., Bosart, L.F. & Schumacher, R.S. (2010) Predecessor rain events ahead of tropical cyclones. *Monthly Weather Review*, 138, 3272–3297.

Gao, W., Zhang, X., Yang, L. & Liu, H. (2010) An improved Sobel edge detection. *In 2010 3rd International conference on computer science and information technology*.

Gershunov, A., Shulgina, T., Ralph, F.M., Lavers, D.A. & Rutz, J.J. (2017) Assessing the climate-scale variability of atmospheric rivers affecting western North America. *Geophysical Research Letters*, 44, 7900–7908.

Gimeno, L., Dominguez, F., Nieto, R., Trigo, R., Drumond, A., Reason, C.J.C. et al. (2016) Major mechanisms of atmospheric moisture transport and their role in extreme precipitation events. *Annual Review of Environment and Resources*, 41, 117–141.

Guan, B. & Waliser, D.E. (2017) Atmospheric rivers in 20 year weather and climate simulations: A multimodel, global evaluation. *Journal of Geophysical Research-Atmospheres*, 122, 5556–5581.

Guo, L., Klingaman, N.P., Vidale, P.L., Turner, A.G., Demory, M.-E. & Cobb, A. (2017) Contribution of tropical cyclones to atmospheric moisture transport and rainfall over East Asia. *Journal of Climate*, 30, 3853–3865.

Hersbach, H., Bell, B., Berrisford, P., Hirahara, S., Horányi, A., Muñoz-Sabater, J. et al. (2020) The ERA5 global reanalysis. *Quarterly Journal of the Royal Meteorological Society*, 146, 1999–2049.

Howse, J. (2013) *OpenCV computer vision with python*. Birmingham, UK: Packt Publishing.

Huffman, D.T.B., George, J., Braithwaite, D., Hsu, K., Joyce, R., Kidd, C. et al. (2020) NASA global precipitation measurement (GPM) integrated multi-satellitE retrievals for GPM (IMERG). *Algorithm Theoretical Basis Document (ATBD) Version*, 6, 4.

Jiang, H. & Zipser, E.J. (2010) Contribution of tropical cyclones to the global precipitation from eight seasons of TRMM data: regional,

seasonal, and interannual variations. *Journal of Climate*, 23, 1526–1543.

Juan, L.I., Xiang-De, X.U., Yue-Qing, L.I., Tian-Liang, Z. & Chong, W.U. (2021) The key supply source of long-distance moisture transport for the extreme rainfall event on July 21, 2012 in Beijing. *Journal of Tropical Meteorology*, 27, 34–47.

Kanopoulos, N., Vasanthavada, N. & Baker, R.L. (1988) Design of an image edge detection filter using the Sobel operator. *IEEE Journal of Solid-State Circuits*, 23, 358–367.

Kim, J., Moon, H., Guan, B., Waliser, D.E., Choi, J., Gu, T.Y. et al. (2020) Precipitation characteristics related to atmospheric rivers in East Asia. *International Journal of Climatology*, 41, E2244–E2257.

Knaff, J.A., Longmore, S.P. & Molenar, D.A. (2014) An objective satellite-based tropical cyclone size climatology. *Journal of Climate*, 27, 455–476.

Kodama, S. & Satoh, M. (2022) Statistical analysis of remote precipitation in Japan caused by typhoons in September. *J. Meteorol. Soc. Jpn.*, 100, 893–911.

Li, X., Wang, C. & Lan, J. (2021) Role of the South China Sea in southern China rainfall: meridional moisture flux transport. *Climate Dynamics*, 56, 2551–2568.

Liang, J. & Yong, Y. (2020) Climatology of atmospheric rivers in the Asian monsoon region. *International Journal of Climatology*, 41, E801–E818.

Liu, B., Tan, X., Gan, T.Y., Chen, X., Lin, K., Lu, M. et al. (2020) Global atmospheric moisture transport associated with precipitation extremes: mechanisms and climate change impacts. *Wiley Interdisciplinary Reviews Water*, 7, e1412.

Liu, F., Wang, B., Ouyang, Y., Wang, H., Qiao, S., Chen, G. et al. (2022) Intraseasonal variability of global land monsoon precipitation and its recent trend. *NPJ Climate and Atmospheric Science*, 5, 1–13.

Liu, Q., Li, T. & Zhou, W. (2021) Impacts of multi-timescale circulations on meridional moisture transport. *Journal of Climate*, 34, 8065–8085.

Lu, M. & Lall, U. (2017) Tropical moisture exports, extreme precipitation and floods in Northeastern US. *Earth Sciences Research Journal*, 6, 91–111.

Mallen, K.J., Montgomery, M.T. & Wang, B. (2005) Reexamining the near-core radial structure of the tropical cyclone primary circulation: implications for vortex resiliency. *Journal of the Atmospheric Sciences*, 62, 408–425.

Manganello, J.V., Hodges, K.I., Kinter, J.L., Cash, B.A., Marx, L., Jung, T. et al. (2012) Tropical cyclone climatology in a 10-km global atmospheric GCM: toward weather-resolving climate modeling. *Journal of Climate*, 25, 3867–3893.

Mei, W., Xie, S.-P., Zhao, M. & Wang, Y. (2015) Forced and internal variability of tropical cyclone track density in the western North Pacific. *Journal of Climate*, 28, 143–167.

Miao, Y., Guo, J., Liu, S., Wei, W., Zhang, G., Lin, Y. et al. (2018) The climatology of low-level jet in Beijing and Guangzhou, China. *Journal of Geophysical Research-Atmospheres*, 123, 2816–2830.

Moore, B.J., Bosart, L.F., Keyser, D. & Jurewicz, M.L. (2013) Synoptic-scale environments of predecessor rain events occurring east of the Rocky Mountains in association with Atlantic Basin tropical cyclones. *Monthly Weather Review*, 141, 1022–1047.

Muszynski, G., Kashinath, K., Kurlin, V. & Wehner, M. (2019) Topological data analysis and machine learning for recognizing atmospheric river patterns in large climate datasets. *Geoscientific Model Development*, 12, 613–628.

Nayak, M.A. & Villarini, G. (2017) A long-term perspective of the hydroclimatological impacts of atmospheric rivers over the Central United States. *Water Resources Research*, 53, 1144–1166.

Pan, M. & Lu, M. (2019) A novel atmospheric river identification algorithm. *Water Resources Research*, 55, 6069–6087.

Pan, M. & Lu, M. (2020) East Asia atmospheric river catalog: annual cycle, transition mechanism, and precipitation. *Geophysical Research Letters*, 47, e2020GL089477.

Park, C., Son, S.W. & Kim, H. (2021) Distinct features of atmospheric rivers in the early versus late east Asian summer monsoon and their impacts on monsoon rainfall. *Journal of Geophysical Research-Atmospheres*, 126, e2020JD033537.

Ralph, F.M., Neiman, P.J., Wick, G.A., Gutman, S.I., Dettinger, M.D., Cayan, D.R. et al. (2006) Flooding on California's Russian River: role of atmospheric rivers. *Geophysical Research Letters*, 33, 2006GL026689.

Ren, F., Gleason, B. & Easterling, D. (2002) Typhoon impacts on China's precipitation. *Advances in Atmospheric Sciences*, 19, 943–952.

Ren, F., Xie, Y., Yin, B., Wang, M. & Li, G. (2020) Establishment of an objective standard for the definition of binary tropical cyclones in the western North Pacific. *Advances in Atmospheric Sciences*, 37, 1211–1221.

Saha, C.K. (2015) Dynamics of disaster-induced risk in southwestern coastal Bangladesh: An analysis on tropical cyclone Aila 2009. *Natural Hazards*, 75, 727–754.

Schumacher, R.S., Galarneau, T.J. & Bosart, L.F. (2011) Distant effects of a recurving tropical cyclone on rainfall in a midlatitude convective system: A high-impact predecessor rain event. *Monthly Weather Review*, 139, 650–667.

Sellars, S.L., Kawzenuk, B., Nguyen, P., Ralph, F.M. & Sorooshian, S. (2017) Genesis, pathways, and terminations of intense global water vapor transport in association with large-scale climate patterns. *Geophysical Research Letters*, 44, 12465–12475.

Shearer, E.J., Nguyen, P., Sellars, S.L., Analui, B., Kawzenuk, B., Hsu, K.L. et al. (2020) Examination of global midlatitude atmospheric river lifecycles using an object-oriented methodology. *Journal of Geophysical Research-Atmospheres*, 125, e2020JD033425.

Shields, C.A., Rutz, J.J., Leung, L.-Y., Ralph, F.M., Wehner, M., Kawzenuk, B. et al. (2018) Atmospheric river tracking method intercomparison project (ARTMIP): project goals and experimental design. *Geoscientific Model Development*, 11, 2455–2474.

Strachan, J., Vidale, P.L., Hodges, K., Roberts, M. & Demory, M.-E. (2013) Investigating global tropical cyclone activity with a hierarchy of AGCMs: the role of model resolution. *Journal of Climate*, 26, 133–152.

Sun, Y., Zhong, Z., Li, T., Yi, L., Hu, Y., Wan, H. et al. (2017) Impact of ocean warming on tropical cyclone size and its destructiveness. *Scientific Reports*, 7, 8154.

Tang, C.K. & Chan, J.C.L. (2014) Idealized simulations of the effect of Taiwan and Philippines topographies on tropical cyclone tracks. *Quarterly Journal of the Royal Meteorological Society*, 140, 1578–1589.

Vincent, R. & Folorunso, O. (2009) A descriptive algorithm for Sobel image edge detection. *In Proceedings of Informing Science & IT Education Conference (InSITE)*, 40, 97–107.

Wang Bin, R.L., Yuqing, W. & Liguang, W. (1999) Dynamics in tropical cyclone motion: A review. *Chinese Journal of Atmospheric Sciences*, 22, 416–434.

Wang, S. & Toumi, R. (2021) Recent migration of tropical cyclones toward coasts. *Science*, 371, 514–517.

Wang, T., Wei, K. & Ma, J. (2021) Atmospheric rivers and Mei-yu rainfall in China: A case study of summer 2020. *Advances in Atmospheric Sciences*, 38, 2137–2152.

Wen, Y., Xue, L., Li, Y., Wei, N. & Lü, A. (2015) Interaction between Typhoon Vicente (1208) and the western Pacific subtropical high during the Beijing extreme rainfall of 21 July 2012. *Journal of Meteorological Research*, 29, 293–304.

Willoughby, H.E. (1990) Temporal changes of the primary circulation in tropical cyclones. *Journal of the Atmospheric Sciences*, 47, 242–264.

Xiong, Y. & Ren, X. (2021) Contribution of atmospheric rivers to precipitation and precipitation extremes in East Asia: diagnosis with moisture flux convergence. *Journal of Meteorological Research*, 35, 831–843.

Xu, G., Ma, X., Chang, P. & Wang, L. (2020) Image-processing-based atmospheric river tracking method version 1 (IPART-1). *Geoscientific Model Development*, 13, 4639–4662.

Xu, G., Osborn, T.J. & Matthews, A.J. (2016) Moisture transport by Atlantic tropical cyclones onto the North American continent. *Climate Dynamics*, 48, 3161–3182.

Xu, H., Duan, Y. & Xu, X. (2022) Indirect effects of binary typhoons on an extreme rainfall event in Henan Province, China from 19 to 21 July 2021: 1. Ensemble-based analysis. *Journal of Geophysical Research-Atmospheres*, 127, e2021JD036265.

Xu, H., Li, X., Yin, J. & Zhang, D. (2023) Predecessor rain events in the Yangtze River Delta region associated with South China Sea and Northwest Pacific Ocean (SCS-WNPO) tropical cyclones. *Advances in Atmospheric Sciences*, 40, 1021–1042.

Yang, L., Liu, M., Smith, J.A. & Tian, F.Q. (2017) Typhoon Nina and the August 1975 flood over central China. *Journal of Hydrometeorology*, 18, 451–472.

Yin, J., Gu, H., Liang, X., Yu, M., Sun, J., Xie, Y. et al. (2022) A possible dynamic mechanism for rapid production of the extreme hourly rainfall in Zhengzhou City on 20 July 2021. *Journal of Meteorological Research*, 36, 6–25.

Ying, M., Zhang, W., Yu, H., Lu, X., Feng, J., Fan, Y. et al. (2014) An overview of the China meteorological administration tropical cyclone database. *Journal of Atmospheric and Oceanic Technology*, 31, 287–301.

Yu, J., Gao, S., Zhang, L., Shen, X. & Guo, L. (2020) Analysis of a remote rainstorm in the Yangtze River Delta region caused by Typhoon Mangkhut (2018). *Journal of Marine Science and Engineering*, 8, 345.

Zhang, A., Chen, Y., Pan, X., Hu, Y., Chen, S. & Li, W. (2022) Precipitation microphysics of tropical cyclones over northeast China in 2020. *Remote Sensing*, 14, 1–17.

Zhou, Y., O'Brien, T.A., Ullrich, P.A., Collins, W.D., Patricola, C.M. & Rhoades, A.M. (2021) Uncertainties in atmospheric river lifecycles by detection algorithms: Climatology and variability. *Journal of Geophysical Research-Atmospheres*, 126, e2020JD033711.

Zuo, H., Chen, Y., Chen, S., Li, W. & Zhang, A. (2022) The effect of the water tower of typhoon Mangkhut (2018). *Atmosphere*, 13, 636.

SUPPORTING INFORMATION

Additional supporting information can be found online in the Supporting Information section at the end of this article.

How to cite this article: Xiao, S., Zhang, A., Chen, Y. & Li, W. (2024) Objective identification of tropical cyclone-induced remote moisture transport using digraphs. *Quarterly Journal of the Royal Meteorological Society*, 150(758), 559–575. Available from: https://doi.org/10.1002/qj.4612